MDPI

Article

Statistical Seismo-Ionospheric Influence with the Focal Mechanism under Consideration

Mei Li [1,*], Zhigao Yang [2], Jin Song [2], Yongxian Zhang [1], Xianghua Jiang [2] and Xuhui Shen [3]

[1]   Institute of Earthquake Forecasting, China Earthquake Administration, Beijing 100036, China
[2]   China Earthquake Networks Center, China Earthquake Administration, Beijing 100045, China
[3]   National Space Science Center, Chinese Academy of Sciences, Beijing 100190, China
[*]   Correspondence: limeixuxl@seis.ac.cn

Abstract: This research aims to statistically investigate seismo-ionospheric influence related to strong earthquakes with different focal mechanisms. The nighttime O^+ density and electron density, measured by the CSES satellite for about 3 years and by the DEMETER satellite for 6 years, were utilized to globally search for ionospheric perturbations with different datasets. Data on strong $M \geq 6.0$ earthquakes with focal mechanism information within a $\pm45°$ geographic latitude were collected during the periods considered. A comparison was automatically performed using software to correlate these ionospheric variations and earthquakes under the condition that a perturbation occurred at a horizontal distance less than 1500 km from the epicenter and up to 15 days before the earthquake. The Kp index was maintained as less than 3 in this timeframe to reduce the effects of geomagnetic activities. Combined with statistical results provided by four groups of rupture and strike-slip earthquakes corresponding to both satellites, it was shown that the averaged ionospheric number of rupture earthquakes is slightly higher than that obtained from strike-slip events, on which basis it seems that, averagely, rupture earthquakes tend to give rise to a heavier influence on the ionosphere than strike-slip ones. Furthermore, this conclusion was comparatively confirmed by commonly detected earthquakes and random events completely for the CSES satellite and partly for the DEMETER satellite. At the same time, we did not gain a firm conclusion regarding the detection rates corresponding to these two types of earthquakes. Thus, further investigations will be necessary as more data are collected.

Keywords: strong earthquake; seismo-ionospheric influence; focal mechanism

1. Introduction

Electromagnetic observation is one of the useful geophysical methods utilized in searching for seismic precursors. Electromagnetic emissions, through ground-based observation, have been reported prior to numerous strong earthquakes (EQs) worldwide, including the 1964 Great Alaska 9.2 EQ [1], the 1989 Loma Prieta 7.1 EQ [2,3], the 1988 Spitak 6.9 EQ [4,5], the 1993 Guam 8.0 EQ [6,7], the 2008 Wenchuan 8.0 EQ [8–10], and the 2011 Japan 9.0 EQ [11]. As the development of Earth observation from space, satellite experiments, due to their large coverage of seismic belts worldwide, fast speed, and high resolution, have gained increasing attention. At the same time, Earth observation from satellites is also characterized by the fact that all satellites have their own revisiting periods. For instance, this period is 5 days for the CSES (China Seismo-Electromagnetic Satellite). Additionally, this leads to a discontinuous measurement of a fixed area, and the observation is dependent on local time (LT). On the one hand, ionospheric abnormities associated with strong EQs have been presented in an increasing number of studies, which have mainly focused on EQ case studies [12–15] and statistical work aiming to reveal the complete temporal-spatial evolution characteristics of plasma variations related to seismic activities [8,16–22].

On the other hand, combined with ground-based data, investigations of lithosphere-atmosphere-ionosphere coupling (LAIC) models and mechanisms have been developing at an unprecedented rate [9,23–29]. The primary study of the LAI coupling mechanism is based on two major hypotheses, namely, the internal gravity wave (IGW) and electric field. In recent years, thermal anomalies, such as ground latent flux and ongoing longwave radiation (OLR), have also been proposed as candidates to interpret the possible mechanism of LAI coupling but lack a well-established model [30]. However, Sorokin and Hayakawa [29] considered that there are some difficulties in the interpretation of observational results of EQ precursors based on the model of IGW propagation due to its propagation properties. Thus, Pulinets and Davidenko [31] argued that it is the smooth transition from acoustic-driven mechanisms to EM coupling. The reason for this is very simple: recently, the acoustic coupling mechanism has shown very low effectiveness, meaning that it is difficult to produce an order of the ionospheric perturbations which are observed before EQs in reality. The LAI coupling model proposed by Kuo et al. [32,33] shows that a current originating from the stressed rock in the focal zone propagates along the magnetic lines from the epicenter area of an earthquake via the ionosphere to its magnetically conjugate point, causing electromagnetic disturbances on the Earth's surface, in the atmosphere, and in the ionosphere and its conjugate point, in that order.

However, the mechanism of earthquakes associated with electromagnetic signals has always been a debated issue that is subject to controversy, since seismo-electromagnetic emissions are presented. Thus far, several theories have been proposed to interpret this mechanism. These include electrokinetic and magnetohydrodynamic effects, piezomagnetism, microfracturing, etc., acting on the production mechanism beneath the Earth [34–37], and chemical channels [38–40], acoustic channels [41–43], electromagnetic channels [24,25], etc., acting on the propagating mechanism in the air as the energy for LAIC. Whatever the production and propagating mechanism is, we must acknowledge that all these properties are attributed to the geodynamics of the Earth; that is, all these phenomena have a close relationship with seismic fault activities. Seismic fault activities are characterized by focal mechanisms involving EQ-related information, such as the strike, dip, and slip of the main fault [44,45]. Among them, slip plays a predominated role in describing fault action styles and determining the impending EQ types, such as normal-fault, reverse-fault, and strike-slip.

In this work, we attempt to statistically investigate the seismo-ionospheric effects of different types of strong EQs. The data utilized in this investigation and the data processing method are introduced in Section 2. In Section 3, the statistical seismo-ionospheric influence results for different types of EQs determined using different datasets derived from the CSES and the DEMETER satellites are exhibited. Additionally, an attempt to confirm these results using randomly generated EQs and commonly detected ones is discussed in Section 4. The discussion and conclusion are provided in Section 5.

2. Description of the Data Processing Method

2.1. Dataset

The investigation was based on data from the DEMETER (Detection of Electro-Magnetic Emissions Transmitted from Earthquake Regions) and the CSES (China Seismo-Electromagnetic Satellite) microsatellites. The DEMETER was launched in 2004 on a quasi-helio-synchronous circular orbit at an altitude of approximately 710 km (decreased to 660 km in December 2005) [46]. The CSES was launched successfully on 2 February 2018 in China. The CSES has a Sun-synchronous circular satellite orbit with an altitude of 500 km, and its descending node operates at 14:00 LT [47]. Both the satellites are continuously powered at geomagnetic latitudes between $-65°$ and $+65°$, providing a fair coverage of the main seismic zones worldwide. We collected the common scientific payloads of ion density and electron density data using an IAP (plasma analyzer instrument) and ISL (Instrument Sonde de Langmuir) [48] onboard DEMETER for approximately 6 years (from December 2004 to November 2010) and using PAP (plasma analyzer package) and LAP

(Langmuir probe) [49] onboard CSES for more than 3 years (from August 2018 to September 2021). The O^+ is the main ion among the ions H^+, He^+, and O^+ detected by the satellites, although it depends on certain factors, such as the local time, altitude, and so on. Thus, only O^+ density data were collected for both satellites in this study. Liu et al. [50] reported a reduced absolute value of the ion density, and the reason for this was that the sensors on the PAP payload were contaminated one month after the CSES launch. The relative variations in the O^+ data have been investigated in scientific research, and positive results have been gained [22,51,52]. Here, only nightside data were utilized, and the Kp index (http://isgi.unistra.fr accessed on 1 January 2022) was also examined to avoid the influences of the geomagnetic activities during all the periods considered in this paper. Li et al. [22] reported that the detection rate and the averaged number of ionospheric perturbations for each detected EQ increased with the time resolution of ionospheric data used. Therefore, in this study, in order to comparably verify the seismo-ionospheric influence of different types of EQs, first, the raw data were resampled with the same time resolutions with respect to the working modes of different satellites: 3 s for the PAP O^+ density and LAP electron density of CSES with respect to their original time resolutions of 0.5 s in the burst mode and 1 s in the survey mode for PAP, being 1.5 s and 3 s for LAP; and 4 s for the IAP O^+ density and ISL electron density of DEMETER with respect to the original time resolutions of 2 s in the burst mode and 4 s in the survey mode for IAP and 1s for ISL. Then, four datasets were obtained: PAP-3s and LAP-3s for the CSES, and IAP-4s and ISL-4s for the DEMETER. Finally, the SAVGOL method was utilized to smooth these datasets so as to eliminate the pulse-like peaks before detecting ionospheric variations. The coefficients of a Savitzky–Golay smoothing filter were gained using the SAVGOL function [53].

According to the GMT catalog (https://www.globalcmt.org/ accessed on 1 January 2022), 797 and 366 strong earthquakes with a magnitude $M_S \geq 6.0$ and within a $\pm 45°$ geographic latitude were derived separately from the DEMETER and CSES periods. Note that M_S has been utilized formally since 25 September 2013, and before that time, there were mainly M_b and, sometimes, M_S in this GMT catalog. Thus, the catalog that we used in this work during the DEMETER period may not have been complete or precise. A limited latitude was selected to avoid the influences of drastic ionospheric variations in electromagnetic properties at high latitudes [54] and some local electromagnetic anomalies, such as the South Atlantic Magnetic Anomaly (SAMA), where more earthquakes are detected with more plasma perturbations but are less reliable [8,21,22]. With little difference from the EQ information utilized in previous work, except for the time, location, depth, and magnitude, each event had some focal mechanism information, such as the strike $\Phi = 0–360°$, dip $\delta = 0–90°$, and slip $\lambda = 0–360°$ of the main fault in this time. Thus, two EQ datasets were constructed, corresponding to the DEMETER and CSES satellites.

2.2. Data Processing Method

The method used here is similar to the one employed previously by Li and Parrot [8,20]. First, the ionospheric perturbations in each dataset (derived from the CSES or DEMETER) are searched globally using a type of software. Only perturbations with a duration of 20–120 s are kept for use. Each ionospheric perturbation is described by several parameters, such as the peak appearance time, orbit, latitude and longitude, amplitude, duration time, and so on.

An example of ionospheric perturbation detected by the software and corresponding to an earthquake is shown in Figure 1. It corresponds to the Menyuan earthquake, which occurred on 8 January 2022 at 01:45:47 CST (China Standard Time), with a magnitude equal to M_S 6.9 and a depth equal to 10 km. Its position was 37.77° N, 101.26° E. Figure 1 shows variations in the electron density.

Figure 1. Fluctuations in electron density registered by the CSES satellite on 28 December 2021, 11 days before the Menyuan M_S 6.9 EQ, Qinghai Province, China. Obvious perturbations related to this Menyuan event are labeled with a black arrow [55].

This ionospheric perturbation acting on the Ne density was successfully detected by the software, and the information is shown in Table 1. From Figure 1 and Table 1, one can see that this ionospheric perturbation occurred 11 days before the Menyuan earthquake at a distance of 120 km away, with an increase in magnitude of 38.4%.

Table 1. Information on the Ne density perturbation shown in Figure 1, which was automatically detected by the software.

Ne Density Perturbation
Time: 2021 12 28 19 3 16 936
Orbit: 21,668
Sub-orbit: 1
Latitude: 38.0043
Longitude: 99.9026
BkgdIon ($\times 10^6/m^3$): 24,798.8
Amplitude ($\times 10^6/m^3$): 34,310.4
Trend: Increase
Percent(%): 38.4
Time_width (m s ms): 1 39 0
Extension (km): 705

The next step is to check whether an ionospheric perturbation corresponds to an EQ or not, with $D \leq 1500$ km and $T \leq 15$ d. Here, D is the distance between the location of this perturbation within the orbit and the epicenter of the EQ, and T is the time delay before the EQ. We eliminate all perturbations that occur when the Kp index is equal to or more than 3 so as to avoid the effects of the geomagnetic activities occurring during this period. If an earthquake is detected by one or more than one perturbation, it is considered as a good detection; if not, it is a bad detection. If a perturbation corresponds to an EQ, it is a true alarm; if not, it is a false alarm. More details can be found in Parrot and Li [38] and Li and Parrot [8,21]. To check the statistical seismo-ionospheric influence, the corresponding ionospheric perturbation number was recorded for each good detection.

3. Statistical Seismo-Ionospheric Influence

Taking focal mechanism information into consideration, with differences between various earthquake types, there are usually three types of earthquakes: normal-fault, reverse-fault and strike-slip, defined in light of the three parameters of strike, dip, and slip [44,45].

Here, there were only 120 normal-fault EQs among 797 EQs during the DEMETER period and 69 among 366 EQs during the CSES period. A small number of samples could not provide a firm result for our topic. For this reason, each good detection dataset was

simply divided into two groups, mainly according to a slip range: strike-slip earthquakes ($\lambda = 0$–$45°$, 136–$225°$, and 316–$360°$) and rupture earthquakes ($\lambda = 46$–$135°$ reverse-fault and 226–$315°$ normal-fault), including 324 and 473 for DEMETER and 162 and 204 for CSES, respectively. First, we detected whether or not each type of EQ corresponded to one or more than one perturbation within an epicentral distance of 1500 km, with 15 d as the time delay before the EQ. We defined several parameters determined earlier by Li and Parrot [8,20], as follows: Ne is the total number of earthquakes, Ng is the number of good detections, which is equal to the number of earthquakes detected, and Np is the number of true alarms, which is equal to the number of perturbations detected. The corresponding values of these parameters for all datasets are displayed in Table 2.

Table 2. Statistical Results Concerning the Seismo-Ionospheric Effects for Different Types of Real EQs Based on Different Datasets Recorded by the CSES and the DEMETER ($D \leq 1500$ km, $T \leq 15$ days).

| | **CSES** | | | | | **DEMETER** | | | | |
| Dataset | **PAP-3s** | | | **LAP-3s** | | | **IAP-4s** | | | **ISL-4s** |
Types	**Ne**	**Ng**	**Np**	**Ng**	**Np**	**Ne**	**Ng**	**Np**	**Ng**	**Np**
Rupture EQs	204	170	1006	128	552	473	266	1453	184	359
Strike-slip EQs	162	150	843	108	444	324	173	909	137	259

Secondly, we calculated the detection rate *r* and the averaged perturbation number *n* for all the good detections of each type of considered event. Before this step, *n* is the average number of corresponding perturbations for each EQ detected, and it is equal to Np divided by Ng, while the detection rate *r* is the ratio between the detected EQs and all the input EQs. The specified results of *n* and *r* derived from Table 2 are presented in Table 3.

Table 3. Statistical Results Related to the Seismo-Ionospheric Effects for Different Types of Real EQs Based on Different Datasets Recorded by the CSES and the DEMETER ($D \leq 1500$ km, $T \leq 15$ days).

| | **CSES** | | | | **DEMETER** | | | |
| Dataset | **PAP-3s** | | **LAP-3s** | | **IAP-4s** | | **ISL-4s** | |
Types	***n***	***r***	***n***	***r***	***n***	***r***	***n***	***r***
Rupture EQs	5.9	83.3%	4.3	62.7%	5.5	56.2%	2.0	38.7%
Strike-slip EQs	5.6	92.6%	4.1	66.7%	5.3	53.4%	1.9	42.3%

For ease of comparison, the data in Table 3 are shown in Figures 2 and 3, respectively, for the averaged perturbation number *n* and the detection rate *r* in the form of histograms.
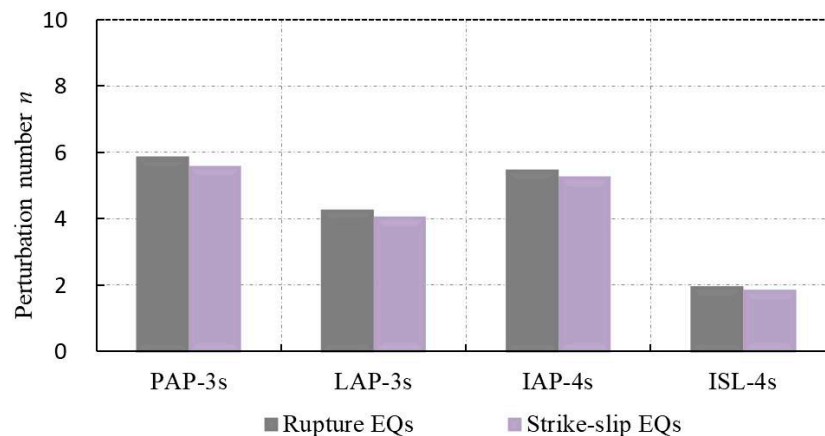

Figure 2. Histogram of averaged perturbation number *n* derived from different datasets of PAP-3s, LAP-3s, IAP-4s, and ISL-4s for different types of real EQs: rupture EQs (light grey bar) and strike-slip EQs (light purple bar).
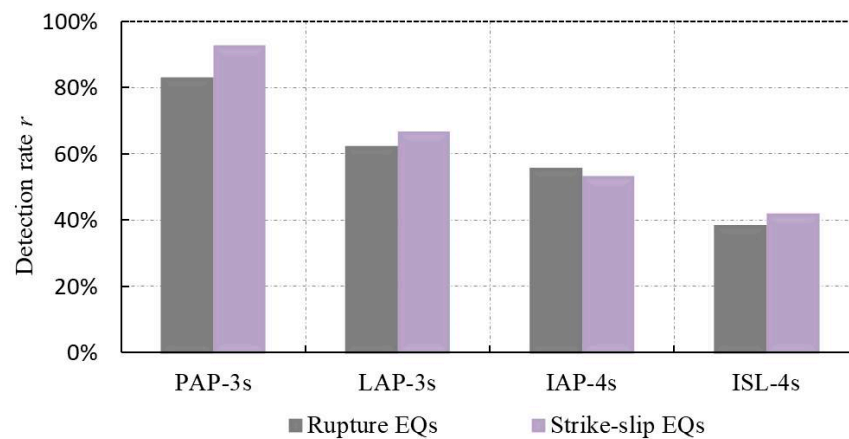
Figure 3. Histogram of the detection rate *r* gained by different datasets of PAP-3s, LAP-3s, IAP-4s, and ISL-4s for different types of real EQs: rupture EQs (light grey bar) and strike-slip EQs (light purple bar).

From Table 3 and Figure 2, one point we can obtain is that the averaged ionospheric perturbation number of rupture EQs (light grey bars) is a little higher than that generated by strike-slip EQs (light purple bars) for all datasets, which means, on average, rupture EQs probably induce ionospheric variations more easily. Additionally, from Table 3 and Figure 2, another point is that, for a given group EQs, for example, the rupture EQs, the perturbation number determined by ion density of IAP on DEMETER (or PAP on CSES) is larger than that of electron density of ISL on DEMETER (or LAP on CSES). It is available for other groups of EQs, too. This result leads to a conclusion that the ion density is more sensitive to seismic activities than the electron density.

However, from Table 3 and Figure 3, the detection rates of strike-slip EQs are higher than that of rupture EQs determined by datasets PAP-3s, LAP-3s and ISL-4s. These results tend to indicate that the strike-slip EQs are detected more easily than rupture ones but this conclusion has not been testified by the IAP-4s dataset, which is of a contrary result that the detection rate determined by strike-slip EQs is a little lower than that of rupture ones.

4. To Confirm the Results

To confirm the results given above that, on average, the number of plasma disturbances induced by rupture EQs is higher than that determined by strike-slip events, but strike-slip EQs tend to be detected more easily, we employee two ways to testify these conclusions. One is to compare with the result generated by random EQs. Another is to examine the averaged perturbation number of strike-slip EQs and rupture ones simultaneously detected by both datasets of PAP-3s and LAP-3s on CSES or of IAP-4s and ISL-4s on DEMETER.

4.1. Comparison with Randomly Generated EQs

A comparison has been performed on random generated EQs to check the validity of the results gained above. In order to obtain random generated events, longitudes of all real EQs within CSES period and DEMETER period have been shifted by $25°$ to the west, and one month has been subtracted to their times [8]. Considering these lists of new events and the ionospheric perturbation database constructed above by different datasets, a detection has been performed under the same conditions as used in Section 2, such as $D \leq 1500$ km, $T \leq 15$ days and Kp ≤ 3. The related parameters of Ne the number of input earthquakes, Ng the number of good detections, and Np the number of right alarms to the randomly generated EQs are listed in Table 4.

Table 4. Statistical Results Related with the Seismo-ionospheric Effects for Different Types of Randomly Generated EQs on Different Datasets Recorded by the CSES and the DEMETER ($D \leq 1500$ km, $T \leq 15$ days).

| Dataset | CSES | | | | | DEMETER | | | | |
| | PAP-3s | | | LAP-3s | | IAP-4s | | | ISL-4s | |
Types	Ne	Ng	Np	Ng	Np	Ne	Ng	Np	Ng	Np
Rupture EQs	204	171	922	118	473	473	258	1463	186	340
Strike-slip EQs	162	141	773	106	442	324	171	901	123	225

The corresponding averaged perturbation number *n* and detection rate *r* calculated from Table 4 for each type of randomly generated EQs have been presented in Table 5.

Table 5. Statistical Results Associated with the Seismo-ionospheric Effects for Different Types of Randomly Generated EQs on Different Datasets Recorded by the CSES and the DEMETER ($D \leq 1500$ km, $T \leq 15$ days).

| Dataset | CSES | | | | DEMETER | | | |
| | PAP-3s | | LAP-3s | | IAP-4s | | ISL-4s | |
Types	*n*	*r*	*n*	*r*	*n*	*r*	*n*	*r*
Rupture EQs	5.4	83.8%	4.0	57.8%	5.7	54.5%	1.8	39.3%
Strike-slip EQs	5.5	87.0%	4.2	65.4%	5.3	52.7%	1.8	38.0%

To compare easily, the data in Table 5 have been shown in Figures 4 and 5, respectively for the averaged perturbation number *n* and the detecting rate *r* under the form of histograms.
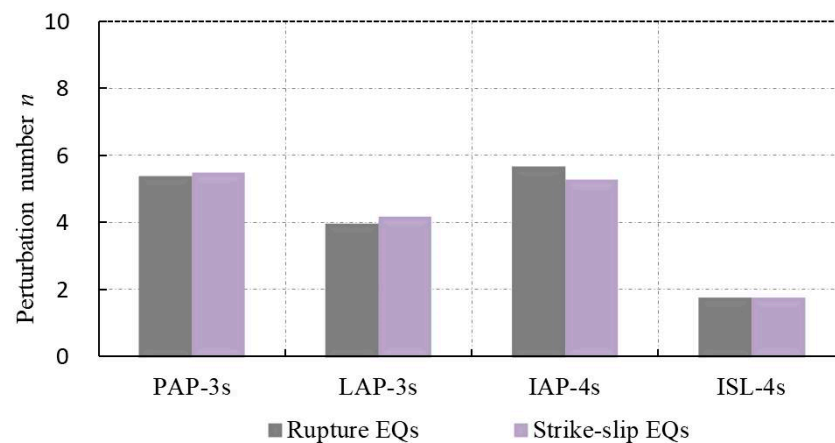

Figure 4. Histogram of averaged ionospheric number *n* derived from different datasets of PAP-3s, LAP-3s, IAP-4s, and ISL-4s for different types of randomly generated EQs: rupture EQs (light grey bar) and strike-slip EQs (light purple bar).

Figure 4 shows that the averaged ionospheric number for the random rupture EQs (light grey bar) is slightly lower than that generated for the random strike-slip EQs based on the CSES datasets of PAP-3s and LAP-3s, which is contrary to that shown in Figure 2. However, this was not observed using the DEMETER IAP-4s and ISL-4s datasets. The averaged numbers attained in this timeframe either show the same variation trend as IAP-4s or maintain balance with ISL-4s for the different types of EQs compared with that exhibited in Figure 2.
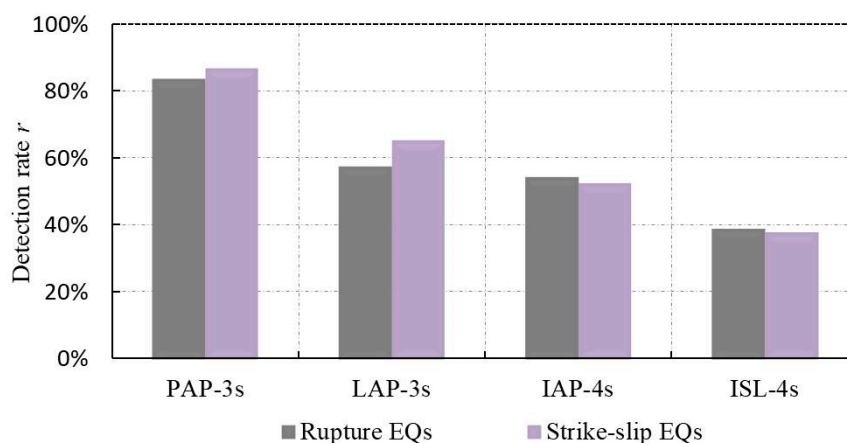
Figure 5. Histogram of the detection rate *r* derived from different datasets of PAP-3s, LAP-3s, IAP-4s, and ISL-4s for different types of randomly generated EQs: rupture EQs (light grey bar) and strike-slip EQs (light purple bar).

Figure 5 exhibits the detection rates derived from the different datasets of PAP-3s, LAP-3s, IAP-4s, and ISL-4s for different types of randomly generated EQs: rupture EQs (light grey bar) and strike-slip EQs (light purple bar). From Figure 5, we cannot derive a firm conclusion or any variation trend due to contrary results for the rupture EQs and strike-slip ones recorded by both CSES and DEMETER.

4.2. Results for Commonly Detected EQs

In previous work, Li et al. [22] found that the detection rates are different for the same EQ set using different ionospheric parameters, such as IAP and ISL. This means that an EQ detected by ion density may not be detected by electron density under the same conditions or vice versa. However, we believe that the corresponding ion perturbations and electron perturbations show more reliability if one EQ is detected at the same time by these two parameters.

In this sense, with the DEMETER 797 EQs considered, we checked the output results of IAP and ISL and found that 200 EQs were commonly detected by these both parameters at the same time, including 77 strike-slip EQs and 123 rupture events. The CSES results for PAP and LAP were also examined, and 219 EQs were detected commonly, covering 101 strike-slip EQs and 118 rupture ones. Their corresponding parameters are displayed in Table 6.

Table 6. Statistical Results Concerning the Seismo-Ionospheric Influences for Different Types of Commonly Detected EQs Based on Different Datasets Recorded by the CSES and the DEMETER ($D \leq 1500$ km, $T \leq 15$ days).

	CSES			DEMETER		
Dataset	**PAP-3s**		**LAP-3s**	**IAP-4s**		**ISL-4s**
Types	**Ng**	**Np**	**Np**	**Ng**	**Np**	**Np**
Rupture EQs	118	626	498	123	697	245
Strike-slip EQs	101	488	412	77	400	147

The averaged ionospheric numbers determined using different datasets for the two commonly detected types of EQs, i.e., rupture EQs and strike-slip ones, were also specified using Np divided by Ng, and their values are listed in Table 7. They are also shown in the histograms in Figure 6.

Table 7. Statistical Results Concerning the Seismo-Ionospheric Influences for Different Types of Commonly Detected EQs Based on Different Datasets Recorded by the CSES and the DEMETER ($D \leq 1500$ km, $T \leq 15$ days).

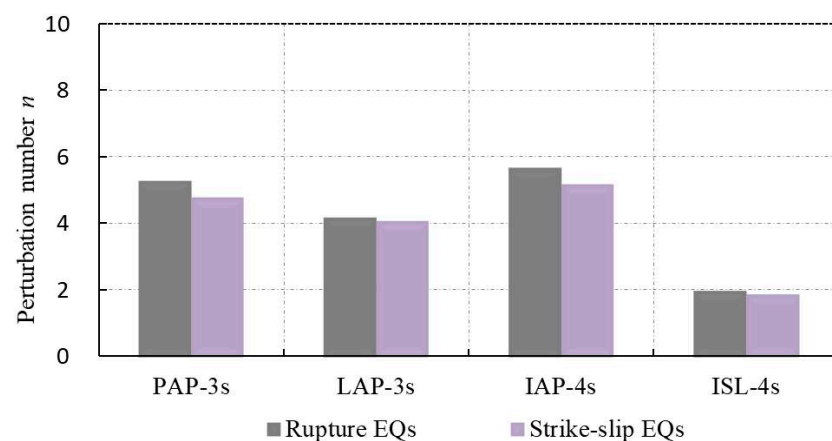| Dataset	CSES		DEMETER	
	PAP-3s	**LAP-3s**	**IAP-4s**	**ISL-4s**
Types	*n*	*n*	*n*	*n*
Rupture EQs	5.3	4.2	5.7	2.0
Strike-slip EQs	4.8	4.1	5.2	1.9

Figure 6. Histogram of averaged perturbation number *n* determined using different datasets of PAP-3s, LAP-3s, IAP-4s, and ISL-4s for commonly detected EQs: rupture EQs (light grey bar) and strike-slip EQs (light purple bar), detected by the CSES satellite and DEMETER satellite, respectively.

From Figure 6, it is clear that for each dataset, the commonly detected rupture EQ list corresponds to higher averaged plasma perturbations (see the light grey bars in Figure 6) than those determined for the strike-slip events (see light purple bars in Figure 6) based on both the CSES satellite and the DEMETER satellite, which is highly consistent with the results displayed in Figure 2 in Section 3.

5. Discussion and Conclusions

From the work outlined above, it seems that rupture EQs (normal-fault EQs and reverse-fault EQs) can prompt more plasma variations than strike-slip EQs. The fact that seismic precursors have a close relationship with focal tectonic backgrounds has been subject to much investigation. As early as 1984, Mogi [56] reported that simple shear movements of faults at a low stress level in California led to less earthquake precursors, while more precursors occurred in the small-scale plate subduction belt in Japan and large-scale intra-plates in China due to high stress levels. On the basis of this work, Mei [57] proposed a theory of rare precursors prior to strike-slip EQs and many precursors to brittle events in light of their different focal mechanisms in China. This conclusion was further testified by Zhang et al. [58], who found that the number of precursors for rupture EQs was larger than that for strike-slip shocks among 31 EQs with a magnitude M_S equal to or more than 5.0 that occurred in southwest China. Using total electron content (TEC) measurements, Cahyadi [59] investigated ionospheric responses to the 26 December 2004 Andaman Sumatra EQ, 11 April 2012 North off Sumatra EQ, and 7 December 2012 North Japan EQ, with different high-angle reverse-fault, strike-slip, and normal-fault focal mechanisms, respectively. The results showed that the initial positive TEC changes in the reverse and normal faults and positive and negative variations in the strike-slip EQs reflect differences in co-seismic vertical crustal displacements. Our statistical results agree well with these previous studies.

To understand this conclusion, we can apply the Mohr-Coulomb (MC) failure criterion and Byerlee law, which are usually utilized to interpret two types of rock failure: fracture and stick-slip [58]. The MC criterion was contributed by Mohr and Coulomb [60]. Fracture means the instability and failure of an intact rock, and the principal stress σ must be beyond the failure strength of rock itself [61]. This process complies with the MC failure criterion and mainly leads to rupture EQs, while stick-slip occurs in the previous planes of failed faults, and this movement must predominately surmount the shear stress τ between the planes of a fault. Most strike-slip EQs are attributed to this process. The Coulomb failure criterion line is always beyond Byerlee law line in the plane, as determined by the normal stress σ and the shear stress τ, which means that the stress level of rock rupture is generally higher than that of the rock's stick-slip strength. Strong stress level can release more energy and yield more precursory information [58].

However, the movement of faults is complex. Mogi [56] also considered that precursors for small-scale subductions in Japan are clearly observable but accumulate within a small range compared with the wide-ranging precursors induced by stick-slip between large-scale planes. This means that a strike-slip EQ can induce ionospheric precursors in a wider area, while a rupture one induces precursory perturbations in an area near to the epicenter. In this sense, it is possible that strike-slip EQs have a higher detection rate but a lower ionospheric number, as we showed in Section 3, but this conclusion is not further specified in this paper. It has been reported that the detection rate of EQs can be affected by different factors, such as the magnitude, hyper-central depth, location, and so on [8,20,22]. Thus, it is also possible that the type of EQ considered does not play a predominant role in this period. At the same time, the scale of seismic faults is also a factor that affects the appearance range of precursors prior to strong EQs. Liu et al. [62] showed that the extreme ionospheric reductions and enhancements extended the spatial distribution by approximately 1650 km in latitude and 2850 km in longitude, respectively, from the 12 May 2008 Wenchuan epicenter. Here, we limit the distance D to 1500 km from the epicenters of the events. Moreover, we simply divide all the EQs meeting the conditions into two groups in light of their slip ranges, i.e., strike-slip EQs and rupture EQs, due to the lower number of normal-fault EQs. Hence, we expect that further research based on increased numbers of samples and details will help us to reveal more evidence on this topic.

However, Chen et al. [63] showed that the situation is more complex. Complex physical processes contribute to the generation of ionospheric precursors. Among the possible sources of variability, it is necessary to consider the geological structure of the region of study and, in particular, the structure of the tectonic faults, the source mechanisms of the given earthquakes (slip, thrust, etc.), the sporadic nature or regularity of the emanations from the ground into the atmosphere, the atmospheric (weather) conditions, regular daily variations in the ionosphere parameters, and the observation point positions in relation to the future epicenter position.

Considering the two ionospheric parameters of ionic density and electronic density measured onboard both the DEMETER and the CSES satellites, as well as the two types of EQs, namely, rupture events and strike-slip ones, which took place within a $\pm 45°$ geographic latitude during the satellite periods, we statistically demonstrated that rupture EQs can have a stronger influence on the ionosphere than strike-slip ones. This conclusion was also further confirmed by randomly generated EQs and EQs commonly detected by CSES, while the condition for DEMETER was slightly different from what we expected when the random list of EQs was used. However, during our work, we also noted that, on the one hand, the EQ catalog derived from the GMT catalog was not complete or not precise during the DEMETER period. Most of the events were M_b and, sometimes, M_S. There is no correct estimation regarding the effect of this catalog. On the other hand, the numbers of collected EQs within a $\pm 45°$ geographic latitude were 797 for DEMETER and 366 for CSES, but their commonly detected EQs were 200 and 218, respectively. As it is well-known that the DEMETER and CSES operate along orbits at different altitudes, it is

possible that they have different properties. Hence, further research will be necessary as more data are gained.

From the analysis above, it was shown that the averaged ionospheric number of rupture earthquakes is slightly higher than that obtained for strike-slip events, which indicates that rupture earthquakes tend to have a stronger influence on the ionosphere than strike-slip ones. To confirm this conclusion, the same statistical work was also conducted on earthquakes commonly detected by both electron density and ion density and on random events. The same conclusion was obtained completely for the CSES satellite but only partly for the DEMETER satellite. Moreover, we did not obtain a firm conclusion regarding the detection rates corresponding to these two types of earthquakes. Thus, further investigations will be necessary as more data are collected.

At the same time, one point that we should mention regarding this work period is that, for a fixed satellite, such as the CSES, the statistical seismo-ionospheric influence of the averaged perturbation number or detection rate determined by the PAP O^+ density is always larger than that of the LAP electron density. This result is also relevant to another satellite, the DEMETER, according to which it seems that ion density is more sensitive to earthquakes than electron density, but this requires further research.

Author Contributions: Writing and editing, M.L.; data collection and investigation, Z.Y., X.J., Y.Z. and J.S.; review, X.S. All authors have read and agreed to the published version of the manuscript.

Institutional Review Board Statement: Institutional review board approval of our institute was obtained for this study.

Informed Consent Statement: Informed consent was obtained from all subjects involved in the study.

Data Availability Statement: The data utilized in this paper are available through the website https://www.leos.ac.cn/ accessed on 1 July 2022.

Conflicts of Interest: The authors declare no conflict of interest.

References

1. Moore, G.W. Magnetic disturbances preceding the 1964 Alaska earthquake. *Nature* **1964**, *203*, 508–509. Available online: http://www.nature.com/articles/203508b0 (accessed on 1 January 2022). [CrossRef]
2. Fraser-Smith, A.C.; Bernardi, A.; McGill, P.R.; Ladd, M.E.; Helliwell, R.A.; Villard, O.G., Jr. Low-frequency magnetic measurements near the epicenter of the M_S 7.1 Loma Prieta earthquake. *Geophys. Res. Lett.* **1990**, *17*, 1465–1468. [CrossRef]
3. Bernardi, A.; Fraser-Smith, A.C.; McGill, P.R.; Villard, O.G., Jr. Magnetic field measurements near the epicenter of the M_S 7.1 Loma Prieta earthquake. *Phys. Earth Planet. Int.* **1991**, *68*, 45–63. [CrossRef]
4. Molchanov, O.A.; Kopytenko, Y.A.; Voronov, P.M.; Kopytenko, E.A.; Matiashvili, T.G.; Fraser-Smith, A.C.; Bernardi, A. Results of ULF Magnetic field measurements near the epicenters of the Spitak (M_S 6.9) and Loma Prieta (M_S 7.1) earthquakes: Comparative analysis. *Geophys. Res. Lett.* **1992**, *19*, 1495–1498. [CrossRef]
5. Kopytenko, Y.A.; Matiashvili, T.G.; Voronov, P.M.; Kopytenko, E.A.; Molchanov, O.A. Detection of ultra-low frequency emissions connected with the Spitak earthquake and its aftershock activity, based on solar pulsations data at Dusheti and Vardzia observatories. *Phys. Earth Planet. Int.* **1993**, *77*, 85–95. [CrossRef]
6. Hayakawa, M.; Kawate, R.; Molchanov, O.A.; Yumoto, K. Results of ultra-low frequency magnetic field measurements during the Guam earthquake of 8 August 1993. *Geophys. Res. Lett.* **1996**, *23*, 241–244. [CrossRef]
7. Kawate, R.; Molchanov, O.A.; Hayakawa, M. Ultra-low frequency magnetic fields during the Guam earthquake of 8 August 1993 and their interpretation. *Phys. Earth Planet. Int.* **1998**, *105*, 229–238. [CrossRef]

8. Li, M.; Parrot, M. Statistical analysis of an ionospheric parameter as a base for earthquake prediction. *J. Geophys. Res. Space Physics* **2013**, *118*, 3731–3739. [CrossRef]
9. Li, M.; Tan, H.; Cao, M. Ionospheric influence on the seismo-telluric current related to electromagnetic signals observed before the Wenchuan M_S 8.0 earthquake. *Solid Earth* **2016**, *7*, 1405–1415. [CrossRef]
10. Li, M.; Yao, L.; Wang, Y.L.; Parrot, M.; Hayakawa, M.; Lu, J.; Tan, H.; Xie, T. Anomalous phenomena in DC–ULF solar daily variation registered three days before the 12 May 2008 Wenchuan M_S 8.0 earthquake. *Earth Planet. Phys.* **2019**, *3*, 330–341. [CrossRef]
11. Ouzounov, D.; Pulinets, S.; Hattori, K.; Taylor, P. (Eds.) *Pre-Earthquake Processes: A Multidisciplinary Approach to Earthquake Prediction Studies*; AGU Geophysical Monograph; Wiley: New York, NY, USA, 2018; 365p.
12. Akhoondzadeh, M.; Parrot, M.; Saradjian, M.R. Electron and ion density variations before strong earthquakes ($M > 6.0$) using DEMETER and GPS data. *Nat. Hazards Earth Syst. Sci.* **2010**, *10*, 7–18. [CrossRef]
13. Zhao, B.; Yu, T.; Wang, M.; Wan, W.; Lei, J.; Liu, L.; Ning, B. Is an unusual large enhancement of ionospheric electron density linked with the 2008 great Wenchuan earthquake? *J. Geophys. Res.* **2008**, *113*, A11304. [CrossRef]
14. Ding, Z.H.; Wu, J.; Sun, S.J.; Chen, J.S.; Ban, P.P. The variation of ionosphere on some days before the Wenchuan Earthquake. *Chin. J. Geophys.* **2010**, *53*, 30–38. [CrossRef]
15. Xu, T.; Hu, Y.L.; Wu, J.; Wu, Z.S.; Suo, Y.C.; Feng, J. Giant disturbance in the ionospheric F2 region prior to the *M* 8.0Wenchuan earthquake on 12 May 2008. *Ann. Geophys.* **2010**, *28*, 1533–1538. [CrossRef]
16. Píša, D.; Němec, F.; Parrot, M.; Santolík, O. Attenuation of electromagnetic waves at the frequency ~1.7 kHz in the upper ionosphere observed by the DEMETER satellite in the vicinity of earthquakes. *Ann. Geophys.* **2012**, *55*, 157–163. [CrossRef]
17. Píša, D.; Němec, F.; Santolík, O.; Parrot, M.; Rycroft, M. Additional attenuation of natural VLF electromagnetic waves observed by the DEMETER spacecraft resulting from preseismic activity. *J. Geophys. Res.* **2013**, *118*, 5286–5295. [CrossRef]
18. Parrot, M. Statistical analysis of the ion density measured by the satellite DEMETER in relation with the seismic activity. *Earthq. Sci.* **2011**, *24*, 513–521. [CrossRef]
19. Parrot, M. Statistical analysis of automatically detected ion density variations recorded by DEMETER and their relation to seismic activity. *Ann. Geophys.* **2012**, *55*, 149–155. [CrossRef]
20. Li, M.; Parrot, M. "Real time analysis" of the ion density measured by the satellite DEMETER in relation with the seismic activity. *Nat. Hazards Earth Syst. Sci.* **2012**, *12*, 2957–2963. [CrossRef]
21. Li, M.; Parrot, M. Statistical analysis of the ionospheric ion density recorded by DEMETER in the epicenter areas of earthquakes as well as in their magnetically conjugate point areas. *Adv. Space Res.* **2018**, *61*, 974–984. [CrossRef]
22. Li, M.; Shen, X.; Parrot, M.; Zhang, X.; Zhang, Y.; Yu, C.; Yan, R.; Liu, D.; Lu, H.; Guo, F.; et al. Primary joint statistical seismic influence on ionospheric parameters recorded by the CSES and DEMETER satellites. *J. Geophys. Res. Space Phys.* **2020**, *125*, e2020JA028116. [CrossRef]
23. De Santis, A.; Franceschi, G.D.; Spogli, L.; Perrone, L.; Alfonsi, L.; Qamili, E.; Cianchini, G.; Giovambattista, R.D.; Salvi, S.; Filippi, E.; et al. Geospace perturbations induced by the Earth: The state of the art and future trends. *Phys. Chem. Earth* **2015**, *85–86*, 17–33. [CrossRef]
24. Hayakawa, M.; Molchanov, O.A. (Eds.) *Seismo-Electromagnetics: Lithosphere-Atmosphere-Ionosphere Coupling*; Terrapub: Tokyo, Japan, 2002.
25. Li, M.; Lu, J.; Zhang, X.; Shen, X. Indications of ground-based electromagnetic observations to a possible lithosphere-atmosphere-ionosphere electromagnetic coupling before the 12 May 2008 Wenchuan M_S 8.0 earthquake. *Atmosphere* **2019**, *10*, 355. [CrossRef]
26. Molchanov, O.; Fedorov, E.; Schekotov, A.; Gordeev, E.; Chebrov, V.; Surkov, V.; Rozhnoi, A.; Andreevsky, S.; Iudin, D.; Yunga, S.; et al. Lithosphere-atmosphere-ionosphere coupling as governing mechanism for preseismic short-term events in atmosphere and ionosphere. *Nat. Hazards Earth Syst. Sci.* **2004**, *4*, 757–767. [CrossRef]
27. Pulinets, S.A.; Boyarchuk, K.A.; Hegai, V.V.; Kim, V.P.; Lomonosov, A.M. Quasielectrostatical model of atmosphere-thermosphere-ionosphere coupling. *Adv. Space Res.* **2000**, *26*, 1209–1218. [CrossRef]
28. Pulinets, S.A.; Ouzounov, D. Lithosphere-Atmosphere-Ionosphere Coupling (LAIC) model-An unified concept for earthquake precursors validation. *J. Southeast Asian Earth Sci.* **2011**, *41*, 371–382. [CrossRef]
29. Sorokin, V.M.; Hayakawa, M. Generation of Seismic–Related DC Electric Fields and Lithosphere-Atmosphere-Ionosphere Coupling. *Modern Appl. Sci.* **2013**, *7*, 1–25. [CrossRef]
30. Hayakawa, M.; Pulinets, S. Lithosphere-atmosphere-ionosphere coupling (laic) model. In *Electromagnetic Phenomena Associated with Earthquakes*; Transworld Research Network: Trivandrum, India, 2009.
31. Pulinets, S.A.; Davidenko, D. Ionospheric precursors of earthquakes and Global Electric Circuit. *Adv. Space Res.* **2014**, *53*, 709–723. [CrossRef]
32. Kuo, C.L.; Huba, J.D.; Joyce, G.; Lee, L.C. Ionosphere plasma bubbles and density variations induced by pre-earthquake rock currents and associated surface charges. *J. Geophys. Res. Space Phys.* **2011**, *116*, A10317. [CrossRef]
33. Kuo, C.L.; Lee, L.C.; Huba, J.D. An improved coupling model for the lithosphere-atmosphere-ionosphere system. *J. Geophys. Res. Space Phys.* **2014**, *119*, 3189–3205. [CrossRef]

34. Draganov, A.B.; Inan, U.S.; Taranenko, Y.N. ULF magnetic signatures at the earth due to groundwater flow: A possible precursor to earthquakes. *Geophys. Res. Lett.* **1991**, *18*, 1127–1130. [CrossRef]

35. Fenoglio, M.A.; Johnston MJ, S.; Byerlee, J.D. Magnetic and electric fields associated with changes in high pore pressure in fault zones: Application to the Loma Prieta ULF emissions. *J. Geophys. Res.* **1995**, *100*, 12951–12958. [CrossRef]

36. Egbert, G.D. On the generation of ULF magnetic variations by conductivity fluctuations in a fault zone. *Pure Appl. Geophys.* **2002**, *159*, 1205–1227. [CrossRef]

37. Simpson, J.J.; Taflove, A. Electrokinetic effect of the Loma Prieta earthquake calculated by an entire-Earth FDTD solution of Maxwell's equations. *Geophys. Res. Lett.* **2005**, *32*, L09302. [CrossRef]

38. Parrot, M.; Li, M. Statistical Analysis of the Ionospheric Density Recorded by the Satellite during Seismic Activity. In *Pre-Earthquake Processes: A Multidisciplinary Approach to Earthquake Prediction Studies*; AGU Monograph by Ouzounov; Pulinets, D.S., Kafatos, M.C., Taylor, P., Eds.; Wiley: New York, NY, USA, 2018; pp. 319–328.

39. Sorokin, V.M.; Chmyrev, V.M.; Hayakawa, M. A review on electrodynamic influence of atmospheric processes to the ionosphere. *Open J. Earthq. Res.* **2020**, *9*, 113–141. [CrossRef]

40. Liperovsky, V.A.; Meister, C.V.; Liperovskaya, E.V.; Bogdanov, V.V. On the generation of electric field and infrared radiation in aerosol clouds due to radon emanation in the atmosphere before earthquakes. *Nat. Hazards Earth Syst. Sci.* **2008**, *8*, 1199–1205. [CrossRef]

41. Hayakawa, M.; Kasahara, Y.; Nakamura, T.; Hobara, Y.; Rozhnoi, A.; Solovieva, M.; Molchanov, O.A.; Korepanov, K. Atmospheric gravity waves as a possible candidate for seismo-ionospheric perturbations. *J. Atmos. Electr.* **2011**, *31*, 129–140. [CrossRef]

42. Korepanov, V.; Hayakawa, M.; Yampolsky, Y.; Lizunov, G. AGW as a seismo-ionospheric coupling responsible agent. *Phys. Chem. Earth* **2009**, *34*, 485–495. [CrossRef]

43. Yang, S.S.; Asano, T.; Hayakawa, M. Abnomal gravity wave activity in the stratosphere prior to the 2016 Kumamoto earthquakes. *J. Geophys. Res. Space Phys.* **2019**, *124*, 1410–1425. [CrossRef]

44. Peter, M.S. *Introduction to Seismology*; Cambridge University Press: Cambridge, UK, 1999; 272p.

45. Stein, S.; Wysession, M. *An Introduction to Seismology, Earthquakes, and Earth Structure*; Blackwell Publishing: Hoboken, NJ, USA, 2003; 510p.

46. Parrot, M.; Berthelier, J.J.; Lebreton, J.P.; Sauvaud, J.A.; Santol'ık, O.; Blecki, J. Examples of unusual ionospheric observations made by the DEMETER satellite over seismic regions. *Phys. Chem. Earth* **2006**, *31*, 486–495. [CrossRef]

47. Shen, X.; Zhang, X.; Yuan, S.; Wang, L.; Cao, J.; Huang, J.; Zhu, X.; Piergiorgio, P.; Dai, J. The state-of-the-art of the China Seismo-Electromagnetic Satellite mission. *Sci. China Technol. Sci.* **2018**, *61*, 634–642. [CrossRef]

48. Berthelier, J.J.; Godefroy, M.; Leblanc, F.; Seran, E.; Peschard, D.; Gilbert, P.; Artru, J. IAP, the thermal plasma analyzer on DEMETER. *Planet. Space Sci.* **2006**, *54*, 487–501. [CrossRef]

49. Yan, R.; Guan, Y.; Shen, X.; Huang, J.; Zhang, X.; Liu, C.; Liu, D. The Langmuir Probe onboard CSES: Data inversion analysis method and first results. *Earth Planet. Phys.* **2018**, *2*, 479–488. [CrossRef]

50. Liu, C.; Guan, Y.; Zheng, X.; Zhang, A.; Piero, D.; Sun, Y. The technology of space plasma in-situ measurement on the China Seismo-Electromagnetic Satellite. *Sci. China Tech. Sci.* **2018**, *62*, 829–838. [CrossRef]

51. Yang, Y.; Zeren, Z.; Shen, X.; Chu, W.; Huang, J.; Wang, Q.; Yan, R.; Xu, S.; Lu, H.; Liu, D. The first intense solar storm event recorded by the China Seismo Electromagnetic Satellite. *Space Weather.* **2020**, *18*, e2019SW002243. [CrossRef]

52. Liu, D.; Zeren, Z.; Shen, X.; Zhao, S.; Yan, R.; Wang, X.; Liu, C.; Guan, Y.; Zhu, X.; Miao, Y.; et al. Typical ionospheric disturbances revealed by the plasma analyzer package onboard the China Seismo-Electromagnetic Satellite. *Adv. Space Res.* **2021**, *68*, 3796–3805. [CrossRef]

53. Savitzky, A.; Golay, M.J.E. Smoothing and differentiation of data by simplified least squares procedures. *Anal. Chem.* **1964**, *36*, 1627–1639. [CrossRef]

54. Yan, R.; Zhima, Z.; Xiong, C.; Shen, X.; Huang, J.; Guan, Y.; Zhu, X.; Liu, C. Comparison of electron density and temperature from the CSES satellite with other space-borne and ground-based observations. *J. Geophys. Res. Space Phys.* **2020**, *125*, e2019JA027747. [CrossRef]

55. Li, M.; Wang, H.; Liu, J.; Shen, X. Two large earthquakes registered by the CSES satellite during its earthquake prediction practice in China. *Atmosphere* **2022**, *13*, 751. [CrossRef]

56. Mogi, K. Fundamental Studies on Earthquake Prediction. In *A Collection of Papers of International Symposium on ISC-SEP*; Seismological Press: Beijing, China, 1984; pp. 375–402.

57. Mei, S.R. Regionalism of earthquake precursors. *Earthq. Res. China* **1985**, *1*, 17–23, (In Chinese with English abstract).

58. Zhang, G.M. On the mechanical cause of regional differences of earthquake precursors. *Earthquake* **1988**, *2*, 1–6, (In Chinese with English abstract).

59. Cahyadi, M.N. Comparison of coseismic ionospheric disturbance waveforms revisited: Strike-slip, normal, and reverse fault earthquake. *Geoid* **2015**, *10*, 104–110. [CrossRef]

60. Nadai, A. *Theory of Flow and Fracture of Solids*; McGraw Hill: New York, NY, USA, 1950.

61. Labuz, J.F.; Zang, A. Mohr–Coulomb Failure Criterion. *Rock Mech. Rock Nngineering* **2012**, *45*, 975–979. [CrossRef]

62. Liu, J.Y.; Chen, Y.I.; Chen, C.H.; Liu, C.Y.; Chen, C.Y.; Nishihashi, M.; Li, J.Z.; Xia, Y.Q.; Oyama, K.I.; Hattori, K.; et al. Seismoionospheric GPS total electron content anomalies observed before the 12 May 2008 M_w7.9 Wenchuan earthquake. *J. Geophys. Res.* **2009**, *114*, A04320. [CrossRef]

63. Chen, Y.I.; Chuo, Y.J.; Liu, J.Y.; Pulinets, S.A. Statistical study of ionospheric precursors of strong earthquakes at Taiwan area. In Proceedings of the XXVI URSI General Assembly, Toronto, ON, Canada, 13–21 August 1999.